

Andrew Harris · Jon Dehn · Matt Patrick ·  
Sonia Calvari · Maurizio Ripepe · Luigi Lodato

## Lava effusion rates from hand-held thermal infrared imagery: an example from the June 2003 effusive activity at Stromboli

Received: 10 November 2003 / Accepted: 11 February 2005 / Published online: 24 June 2005  
© Springer-Verlag 2005

**Abstract** A safe, easy and rapid method to calculate lava effusion rates using hand-held thermal image data was developed during June 2003 at Stromboli Volcano (Italy). We used a Forward Looking Infrared Radiometer (FLIR) to obtain images of the active lava flow field on a daily basis between May 31 and June 16, 2003. During this time the flow field geometry and size (where flows typically a few hundred meters long were emplaced on a steep slope) meant that near-vertical images of the whole flow field could be captured in a single image obtained from a helicopter hovering, at an altitude of 750 m and  $\sim 1$  km off shore. We used these images to adapt a thermally based effusion rate method, previously applied to low and high spatial resolution satellite data, to allow automated extraction of effusion rates from the hand-held thermal infrared imagery. A comparison between a thermally-derived ( $0.23\text{--}0.87\text{ m}^3\text{ s}^{-1}$ ) and dimensionally-derived effusion rate ( $0.56\text{ m}^3\text{ s}^{-1}$ ) showed that the thermally-derived range was centered on the expected value. Over the measurement period, the mean effusion rate was  $0.38\pm 0.25\text{ m}^3\text{ s}^{-1}$ , which

is similar to that obtained during the 1985–86 effusive eruption and the time-averaged supply rate calculated for normal (non-effusive) Strombolian activity. A short effusive pulse, reaching a peak of  $\sim 1.2\text{ m}^3\text{ s}^{-1}$ , was recorded on June 3, 2003. One explanation of such a peak would be an increase in driving pressure due to an increase in the height of the magma contained in the central column. We estimate that this pulse would require the magma column to attain a height of  $\sim 190$  m above the effusive vent, which is approximately the elevation difference between the vent and the floor of the NE crater. Our approach gives an easy-to-apply method that has the potential to provide effusion rate time series with a high temporal resolution.

**Keywords** Forward Looking InfraRed (FLIR) · Effusion Rate · Stromboli

Editorial responsibility: M. Carroll

A. Harris (✉) · M. Patrick  
HIGP/SOEST, University of Hawai'i,  
2525 Correa Road,  
Honolulu, HI 96822, USA  
e-mail: harris@higp.hawaii.edu  
Tel.: +808-956-3157  
Fax: +808-956-6322

J. Dehn  
Alaska Volcano Observatory, Geophysical Institute, University  
of Alaska Fairbanks,  
Fairbanks, AK 99775-7320, USA

S. Calvari · L. Lodato  
Istituto Nazionale di Geofisica e Vulcanologia,  
Piazza Roma 2,  
95123 Catania, Italy

M. Ripepe  
Dipartimento di Scienze della Terra, Università di Firenze,  
Via La Pira 4,  
50121 Firenze, Italy

### Introduction

A new effusive eruption began at Stromboli Volcano (Aeolian Islands, Italy) on December 28, 2002. Effusive activity continued until July 22, 2003 and built a  $\sim 170$  m diameter shield abutting the NE edge of the crater terrace (Fig. 1). Tubes and channels extending from this shield fed a compound, dominantly 'a'a, flow field on the northern edge of the Sciara del Fuoco. The flow field was thus emplaced on the  $\sim 30^\circ$  steep slope of the Sciara, where flow front collapses to feed hot grain flows were, at times, almost continuous. The difficulty and hazards of close approach to the region meant that, by May 2003, no ground-based effusion rate measurements had been made. The master channels could not be approached and so the cross-sectional area and velocity measurements, which involve obtaining a depth and width for lava flowing in a channel (Calvari et al. 2002), could not be made. This made this eruption a perfect target for effusion rate calculations using thermal imaging data (e.g. Harris et al. 1997, 1998).

The geometry and size of this flow field, where flows typically a few hundred meters long were emplaced on

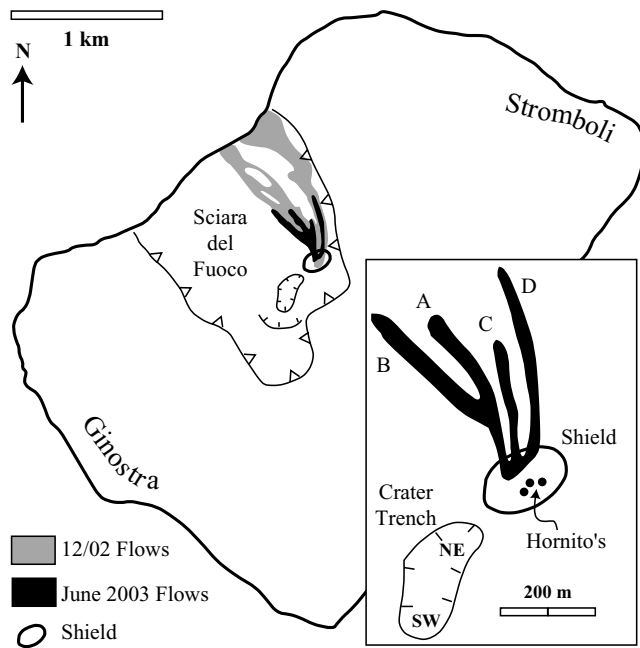


**Fig. 1** Flow field location map and (inset) flow field sketch map for the period May 31–June 16, 2003, indicating the location of the 4 main flow units

a steep and more or less even slope, made collection of thermal image data extremely easy. In this regard, the whole flow field could be captured in a single image obtained from a helicopter hovering  $\sim 1$  km off shore. Thus we used a Forward Looking Infrared Radiometer (FLIR) to obtain images of the flow field on a daily basis between May 31 and June 16, 2003. We used these images to adapt the thermally based effusion rate method, previously applied to low and high spatial resolution satellite data, to allow automated extraction of effusion rates from the hand-held thermal infrared imagery. Here we focus on using data from this 17-day-long case study to describe this technique and to demonstrate how it can be used to provide timely data during an on-going eruption crisis.

### The FLIR: Capabilities and Image Acquisition

The FLIR has been used at Stromboli since 2001 (Dehn et al. 2004), and was employed during the December 2002–July 2003 effusive eruption to contribute to monitoring efforts at Stromboli (Calvari et al. 2004). The FLIR is an uncooled microbolometer that detects emitted radiation in the 7.5–11.5  $\mu\text{m}$  waveband. The instrument is capable of acquiring a  $320 \times 240$  pixel image every 2 s, and the  $24 \times 18^\circ$  field of view of the lens equates to a  $0.075 \times 0.1^\circ$  pixel. Over the typical 1–2 km line of sight distances considered in this study, this gives pixel diameters of 1.3–2.6 m. An internal calibration means that, if distance to target, ambient temperature, humidity and emissivity are inputs, then the temperatures corrected for atmospheric and emissivity effects are the outputs. Here, air temperature and humidity are measured in situ and are input at the start of each measurement

run. In addition, the path length is calculated from the difference between the GPS obtained helicopter position and the known position of the flow field. The FLIR camera software then runs an automated atmospheric and emissivity correction based on the LOWTRAN atmospheric model (Kneizys et al. 1983). The FLIR thus produces digital data that can be rigorously used to determine temperatures of specific targets, calculate thermal flux, and thus effusion rates.

Two FLIRs were used at Stromboli during May 31–June 16, 2003. The first was a FLIR Systems Thermacam 695 maintained by the Istituto Nazionale di Geofisica e Vulcanologia (INGV, Catania, Italy). The second was a FLIR Systems Thermacam 595 maintained by the Alaska Volcano Observatory (AVO). Comparisons were performed between the two instruments by targeting them on a common high temperature source. The instruments performed well and gave comparable data with an error of 15% between the two instruments (total number of measurements = 100, two runs onto hot plate with  $\sim 1$  measurement every 5–10°C between 80 and 500°C as the hot plate heats up).

Daily helicopter flights at an altitude of  $\sim 1$  km were made to gather thermal data for the flow field as well as for the summit craters. Each day, the same flight path was followed with observation points fixed using a hand-held GPS. This also allowed the calculation of the distance to target necessary for atmospheric correction and pixel size calculations. During each flight over the field, FLIR images, centered on the flow field, were acquired from an altitude of 750 m at three locations. These were 0.75, 1.5 and 2 km distant from the flow field. The orientation of the flow field (on a  $\sim 30^\circ$  slope) meant that this location, although not directly above the flow field, effectively allowed collection of flow-wide thermal images with the properties of a vertically acquired image (i.e. the view was perpendicular) and without having to fly at any great altitude (Fig. 2). Next, oblique images of the summit craters (850 m a.s.l.) were acquired from a flying altitude of  $\sim 1500$  m.

### Methodology

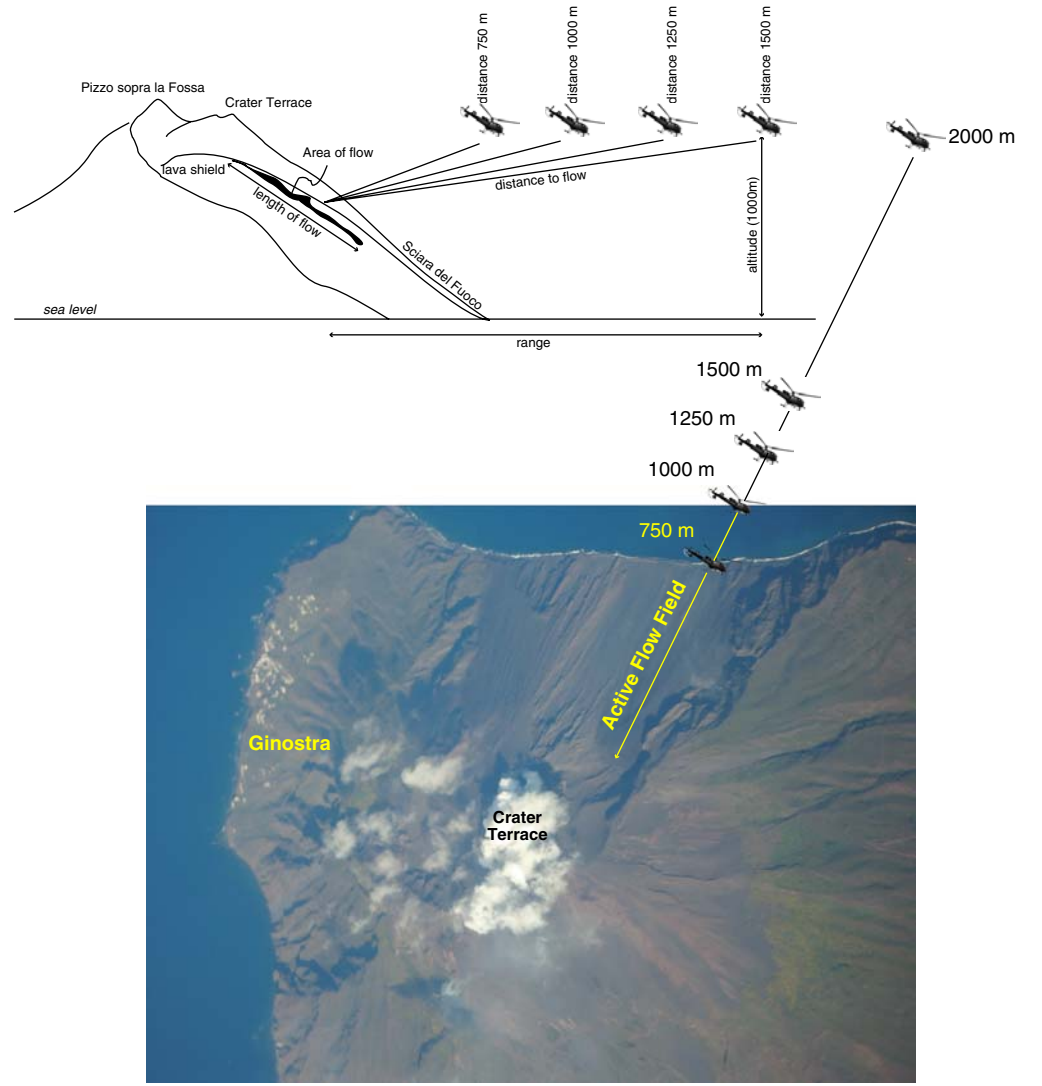
#### Underlying rationale

The effusion rate calculation methodology adapts the approach of Pieri and Baloga (1986) and Crisp and Baloga (1990) to obtain effusion rates ( $E_r$ ). This was previously adapted to extract effusion rates from satellite-derived thermal data (Harris et al. 1997, 1998, 2000). The technique assumes that, in cooling from the eruption temperature ( $T_{\text{erupt}}$ ) to the temperature at which flow motion ceases ( $T_{\text{stop}}$ ), the heat loss (in  $\text{J s}^{-1}$ ) from the flow ( $Q_{\text{out}}$ ) is balanced by heat supplied ( $Q_{\text{in}}$ ), i.e.  $Q_{\text{in}} = Q_{\text{out}}$ . Heat supplied comes from advected heat ( $Q_{\text{adv}}$ ) and latent heat of crystallization ( $Q_{\text{cryst}}$ ), where:

$$Q_{\text{adv}} = E_r \rho c_p (T_{\text{erupt}} - T_{\text{stop}}) \quad (1)$$

$$Q_{\text{cryst}} = E_r \rho f L \quad (2)$$

**Fig. 2** Schematic summarizing helicopter 0–1.5 km flight path and viewing geometry during FLIR data acquisition, with full 2 km flight plan shown in plan view on vertical aerial photo of Stromboli acquired during July 2004



Here  $\rho$ ,  $c_p$ ,  $f$  and  $L$  are lava density, specific heat capacity, mass fraction of post eruption crystallization and latent heat of crystallization, respectively (for values see Table 1). Heat lost can be described by radiation ( $Q_{\text{rad}}$ ), convection ( $Q_{\text{conv}}$ ) and conduction through the flow base ( $Q_{\text{cond}}$ ), where:

$$Q_{\text{rad}} = A \sigma \varepsilon T^4 \quad (3)$$

$$Q_{\text{conv}} = A H_c (T - T_{\text{amb}}) \quad (4)$$

$$Q_{\text{cond}} = A k [(T_{\text{core}} - T_{\text{base}})/h] \quad (5)$$

Here,  $\sigma$ ,  $\varepsilon$ ,  $A$  and  $T$  are the Stefan Boltzmann constant, surface emissivity, lava area and surface temperature (in Kelvin), respectively (for values see Table 1). In Eq. (4),  $H_c$  and  $T_{\text{amb}}$  are the convective heat transfer coefficient and ambient air temperature, respectively. Finally, in Eq. (5),  $k$ ,  $T_{\text{core}}$ ,  $T_{\text{base}}$  and  $h$  are the lava thermal conductivity, core temperature, basal contact temperature and thickness of the thermal boundary layer, respectively.

Now, if we combine Eqs. (1–5), i.e.  $Q_{\text{adv}} + Q_{\text{cryst}} = Q_{\text{rad}} + Q_{\text{conv}} + Q_{\text{cond}}$  we obtain:

$$E_r \rho [c_p(T_{\text{erupt}} - T_{\text{stop}}) + f L] = A \sigma \varepsilon T^4 + A H_c (T - T_{\text{amb}}) + A k [(T_{\text{core}} - T_{\text{base}})/h] \quad (6)$$

Rearranging now allows us to calculate eruption rate,  $E_r$ , from:

$$E_r = Q_{\text{tot}} / \rho [c_p \Delta T + f L] \quad (7)$$

Where, to simplify this equation, we have written  $\Delta T$  for  $T_{\text{erupt}} - T_{\text{stop}}$  and  $Q_{\text{tot}} = Q_{\text{rad}} + Q_{\text{conv}} + Q_{\text{cond}}$ .

This method uses the heat flux (in  $\text{J s}^{-1}$ ) to obtain the volume flux (in  $\text{m}^3 \text{s}^{-1}$ ) using the balance between heat sinks and sources as the body cools across a given temperature range ( $\Delta T$ ). As shown by Wooster et al. (1997), Eq. (7) can be rewritten in terms of total energy lost (in J) and volume ( $\text{m}^3$ ). In this case, the total energy lost ( $E$ ) as the body cools from eruption temperature to ambient is used to estimate the lava volume ( $V$ ) necessary to generate

**Table 1** Model input parameters

Parameter	Description	Value
Ves	Vesicularity	22%
$\rho$	Lava density*	2600 kg m <sup>-3</sup>
$C_p$	Lava specific heat capacity	1225 J kg <sup>-1</sup> K <sup>-1</sup>
$\Delta T$	$T_{\text{erupt}} - T_{\text{stop}}$	150–250°C
$f$	Mass fraction of post-eruption crystallization	45%
$L$	Latent heat of crystallization	$3.5 \times 10^5$ J m <sup>-3</sup>
$\sigma$	Stefan-Boltzmann constant	$5.67 \times 10^{-8}$ W m <sup>-2</sup> K <sup>-1</sup>
$\varepsilon$	Emissivity	0.95
$A$	Lava Area	FLIR-image (m <sup>2</sup> )
$T$	Lava surface temperature	FLIR-image (°C)
$h_c$	Convective heat transfer coefficient	10–100 W m <sup>-2</sup> K <sup>-1</sup>
$T_{\text{amb}}$	Ambient air temperature	20 °C
$k$	Lava thermal conductivity	1.5 W m <sup>-2</sup> K <sup>-1</sup>
$T_{\text{core}}$	Lava core temperature	1000°C
$T_{\text{base}}$	Basal contact temperature	500°C
$h$	Thickness of thermal boundary layer	1 m

\*These are dense rock values. Bulk values are used, i.e. vesicle corrected values

the required energy [ $E = \rho V (c_p \Delta T_2 + f L)$ ]. In this case  $\Delta T_2$  is the cooling range from eruption temperature to ambient (Wooster et al. 1997). In the former case the area of active flows across which  $\Delta T$  applies is identified and the heat flux is calculated to approximate  $E_r$ . In the second case, total energy liberated in cooling through  $\Delta T_2$  (heat flux integrated through time) is used to approximate  $V$ . Thus the former method requires that heat flux from only active flows be used (Harris et al. 1997, 1998; Wright et al. 2001), whereas the latter requires calculation of heat loss from all flows during their entire, until every unit has cooled to ambient (Wooster et al. 1997)

### Setting the equation parameters

Inspection of Eqs. (1)–(7) reveals that, in order to calculate  $E_r$ , we must assume or measure the values for a number of other parameters. The assumed values that we have used here are given in Table 1. These are taken from Harris et al. (2000) and proved to be reasonable values in calibrating this technique using thermal data for Etna and Krafla, as well as Stromboli (see also Harris et al. 1998). Note that the only measured values in Eq. (6) are now lava surface temperature (in Kelvin) and area (in m<sup>2</sup>). These are obtained using the FLIR images as follows.

Identifying the active lava area required by setting of a temperature threshold that would determine whether or not a pixel contained active lava. To set this threshold, we first collected images from a vantage point that was as close as possible to the flow field (750 m distance), as well as perpendicular to the flow, i.e. from an altitude roughly level with the flow field center (~750 m a.s.l.). A manual inspection of the image, guided by visual observations and digital photographs, showed that a threshold of 300 °C successfully flagged all of the active lava pixels. With increased distances from the flow, the increasing size of the pixel will cause pixel integrated temperatures to decline. Thus, to obtain the same lava area from images acquired

at greater distances (1.5–2 km) a lower threshold of 110–200 °C was required. In order to obtain an automated threshold, we collected images over a range of distances: at 250 m steps between a distance of 750 m and 2.5 km, the maximum recommended operating range for the FLIR (Fig. 2). This was done under good (clear) conditions and poor (hazy, cloudy) conditions. At each step, we iterated on temperature until the area extracted from the master image obtained at the 750 m distance was obtained. This gave us the threshold temperature ( $T_{\text{thresh}}$ , in Kelvin) for each distance, where plotting  $T_{\text{thresh}}$  with distance allowed us to define a best-fit relationship for these two parameters. Thus the threshold level for successful active lava area determination was set depending on distance to the target ( $d$ ) and viewing conditions where  $T_{\text{thresh}}$  was obtained, for good and bad conditions, respectively:

$$T_{\text{thresh}} = -0.00003d^2 + 0.029d + 293 \quad (8a)$$

$$T_{\text{thresh}} = -0.123d + 389 \quad (8b)$$

Note that these equations and threshold levels will only apply to our study period and location, and are set to identify areas of currently active flows only. Thus zones of warm, recent but stationary, cooling flows are excluded. This methodology would have to be re-applied and new equations derived for different times and locations.

As argued by Wright et al. (2001), and because area and temperature become our main variables, we are calculating a reasonable slope and intercept in a relationship that relates lava effusion rate to these two variables. Here, Wright et al. (2001) point out that this method relies on first obtaining an approximation for the area of active, moving flows. Next a calculation is applied that assumes that flow area is directly related to eruption rate. The implicit assumption is thus that: changes in the rate at which lava added to the flow field are accommodated by changes in the area of active areas within the flow field, so that eruption rate ( $E_r$ ) and

active flow area ( $A$ ) are positively correlation ( $E_r = m A$ ). Thus we may be able to simplify Eq. (7) to:

$$E_r = m Q_{\text{tot}} - c \quad (9)$$

where  $m$  and  $c$  are the slope and intercept of a linear relationship between  $E_r$  and  $Q_{\text{tot}}$ . Following Wright et al. (2001) it is probably more accurate to consider  $E_r$  as a time-averaged eruption rate rather than an instantaneous effusion rate. Here, the slope and intercept are defined by our assumed input values used for the calculation of the heat flux terms (Table 1). Because there are uncertainties in these values we set them over plausible ranges, and thus obtain ranges of both  $m$  and  $c$ .

The most contentious assumptions in calculating  $Q_{\text{tot}}$  are in the setting of values for  $\Delta T$ ,  $H_c$  and  $Q_{\text{cond}}$ . A lava cooling range ( $\Delta T$ ) of 150–250°C has empirically been shown to be a reasonable range by Pieri and Baloga (1986), and produced good results when applied to other thermal data sets (Harris et al. 1998, 2000). In the setting of the convective heat transfer coefficient ( $h_c$ ) Keszthelyi and Denlinger (1996), Patrick (2002) and Keszthelyi et al. (2003) have shown that values in the range 10–100 W m<sup>-2</sup> K<sup>-1</sup> are reasonable for active lava. Thus we calculated two values for  $Q_{\text{conv}}$ : a minimum value ( $Q_{\text{conv}1}$ ) using  $h_c = 10$  W m<sup>-2</sup> K<sup>-1</sup> and a maximum value ( $Q_{\text{conv}2}$ ) using  $h_c = 100$  W m<sup>-2</sup> K<sup>-1</sup>. These in turn are used with two values of  $\Delta T$ , 150 and 250°C. In calculating  $Q_{\text{cond}}$ , we assume core temperature, base temperature and thickness of the thermal boundary layer. A minimum value for  $Q_{\text{cond}}$  of zero is obtained if  $T_{\text{core}} = T_{\text{base}}$ . A maximum value is obtained using the values for  $T_{\text{core}}$ ,  $T_{\text{base}}$  and  $h$  given in Table 1. Thus we also set our range of  $Q_{\text{tot}}$  (and hence  $E_r$ ) estimates using the minimum and maximum expected conductive heat loss.

As a result of the above considerations we prefer to quote our eruption rate estimates as a range constrained by the uncertainty in the input parameters. The minimum value considers only  $Q_{\text{rad}} + Q_{\text{conv}1}$  and a  $\Delta T$  value of 250°C in the calculation of  $Q_{\text{tot}}$ . The maximum values considers  $Q_{\text{rad}} + Q_{\text{conv}2} + Q_{\text{cond}}$  with a  $\Delta T$  value of 150°C. These values give the following limits for the relationship between  $E_r$  and  $Q_{\text{tot}}$  in Eq. (9):

$$E_r(\text{min}) = 2 \times 10^{-9} Q_{\text{tot}}(\text{min}) - 0.016 \quad (10a)$$

$$E_r(\text{max}) = 1 \times 10^{-9} Q_{\text{tot}}(\text{min}) - 0.0004 \quad (10b)$$

### Eruption rates and error

The entire routine was automated allowing active lava areas, heat fluxes and effusion rates to be made available in real-time. This was achieved using two sets of software written in MATLAB and in the Thermacam Researcher software, respectively (Appendix A). Effusion rates obtained during our study period are given in Table 2. To validate these results we made an independent estimate of effusion rate during May 31, a date when a well-defined master channel was active feeding one of four active lobes.

The channel was 4 m wide ( $w$ ). Assuming that the channel is rectangular-to-semi-circular in cross-section, depth ( $h$ ) can be approximated from  $w/2$ , this gives a 2 m depth and a 8 m<sup>2</sup> cross-sectional area. Now, mean velocity ( $V$ ) can be estimated using Jeffreys Equation (Jeffreys 1925):

$$V = h^2 \rho g \sin(\alpha) / 3\eta \quad (11)$$

in which  $g$  is acceleration due to gravity (9.81 m s<sup>-2</sup>) and  $\eta$  is viscosity [calculated as 10<sup>5</sup>–10<sup>6</sup> Pa s for the shallow system (Marchetti et al. 2004)]. Over a slope of 32° this gives a velocity of 0.2–0.02 m s<sup>-1</sup>, which in yields an effusion rate of 0.14–1.6 m<sup>3</sup> s<sup>-1</sup> for this lobe. This compares with a thermally-derived range of 0.23–0.87 m<sup>3</sup> s<sup>-1</sup>. Further comparisons between FLIR-derived as well as satellite-data-derived and ground-based eruption rates are given in Calvari et al. (2005). These results show a good correlation between the three independent data sets, where the correlation between the between FLIR-derived as well as satellite-derived eruption rates has an  $R^2$  of 0.8 (Calvari et al. 2005).

Given the good fit between these data sets, and following the argument of Wright et al. (2001) it seems likely that we have calibrated the relationship between eruption rate and active flow area. This backs up the work of Pieri and Baloga (1986) and shows that in calibrating this relationship a value of 150–250°C for the main unknown parameter in Eq. (7), i.e.  $\Delta T$ , provides a good empirical fit between eruption rate and active flow area. In other words, suitable slope and intercept values for Eqs. (8a) and (8b) are obtained using  $\Delta T$  of 150–250°C, such that when reasonable area values are input, a range of  $E_r$  are output that embrace the true value (Wright et al. 2001).

By comparing multiple images acquired from the same vantage point and at the same time, we were able to replicate the FLIR-derived lava areas to within 13–17%. These differences can be explained by slight differences in the pixel location between images. While this gives an error on the entire calculation of about  $\pm 0.2$  m<sup>3</sup> s<sup>-1</sup>, the uncertainty in input parameters gives us a range in our output effusion rate of  $\sim 0.64$  m<sup>3</sup> s<sup>-1</sup>.

## Results

During our field study, the flow field could be split into two morphologically distinct sections: a vent area (across the proximal shield) and a flow zone (Flows A–D) (Fig. 1). Use of the FLIR allowed us to chart the evolution of this flow field, to measure its dimensions and apply rheological calculations, and to track the effusion rates.

### Lava flow field morphology and evolution (May 31–June 16)

The vent area comprised a 60×170 m shield, emplaced in the bench at the eastern head of the Sciara del Fuoco and at the foot of the NE crater. The shield was capped by three hornitos. On June 1, semi-persistent lava spattering

**Table 2** Summary of flow lengths (rounded to the nearest 10 m) and effusion rates, N/A = not active. Mid-points for the effusion rate range is given, where the range in each case is  $\pm 50\%$

Date (2003)	Unit A Length (m)	Unit B Length (m)	Unit C Length (m)	Unit D Length (m)	$E_r$ ( $\text{m}^3 \text{s}^{-1}$ )
May 31 (am)	145	N/A	N/A	270	0.60
June 1 (am)	500	320	N/A	420	0.80
June 1 (pm)	140	140	N/A	N/A	0.10
June 2 (am)	200	410	N/A	N/A	0.50
June 3 (am)	280	240	N/A	N/A	1.20
June 4 (am)	200	100	N/A	N/A	0.46
June 4 (pm)	420	80	N/A	N/A	0.39
June 5 (am)	475	120	N/A	N/A	0.50
June 6 (am)	430	105	60	N/A	0.20
June 7 (am)	560	80	N/A	N/A	0.41
June 8 (am)	460	N/A	N/A	N/A	0.31
June 9 (am)	360	40	N/A	N/A	0.24
June 10 (am)	360	40	N/A	N/A	0.31
June 11 (am)	350	N/A	220	90	0.22
June 11 (pm)	400	N/A	150	40	0.14
June 12 (am)	530	N/A	150	N/A	0.31
June 13 (am)	460	N/A	N/A	N/A	0.28
June 13 (pm)	480	N/A	40	N/A	0.25
June 14 (am)	430	N/A	40	N/A	0.16
June 15 (am)	460	N/A	40	N/A	0.41
June 16 (am)	190	N/A	N/A	N/A	0.18
Mean	380	160	100	205	0.38
Standard Dev	110	130	70	210	0.25

from the largest of the three hornitos fed a short (32 m long) channelized 'a'a flow down the hornito flank (Fig. 3). Other zones in the south west sector oozed short-lived pads of slabby pahoehoe. One pad, for example, was active for 30 min beginning 10:50 a.m. (all times are local, = GMT + 1) on June 1. As a result, the surface of the shield comprised a complex, compound flow field of 'a'a and slabby pahoehoe lava (Fig. 3). Numerous, ephemeral vents were active on the north western edge of the shield, where the alignment of these sources pointed to an arcuate zone extending along the north west edge of the shield as the main source area for most lava flow. From this zone, bifurcating channels and tubes extended in a north west direction to feed the main flow zone on the Sciara (Fig. 4).

The flow zone comprised a compound 'a'a flow field in the eastern sector of the Sciara del Fuoco (Fig. 1). Individual units within this flow zone were typically channel-fed, and were emplaced on the  $\sim 30^\circ$  slopes of the Sciara. The angle of the slope resulted in almost continuous crumbling of the active flow fronts to feed hot grain flows and rock flows that extended to the sea.

During the observation period, flows were active in four zones across the flow field (Fig. 1):

1. The north-eastern edge (Unit D)
2. The central sector NE edge (Unit C)
3. The central sector SW edge (Unit A)
4. The south-west edge (Unit B).

Activity at each of these units is summarized in Table 2 where, during the observation period, flows extended typically a few hundred meters from the shield, fed by an

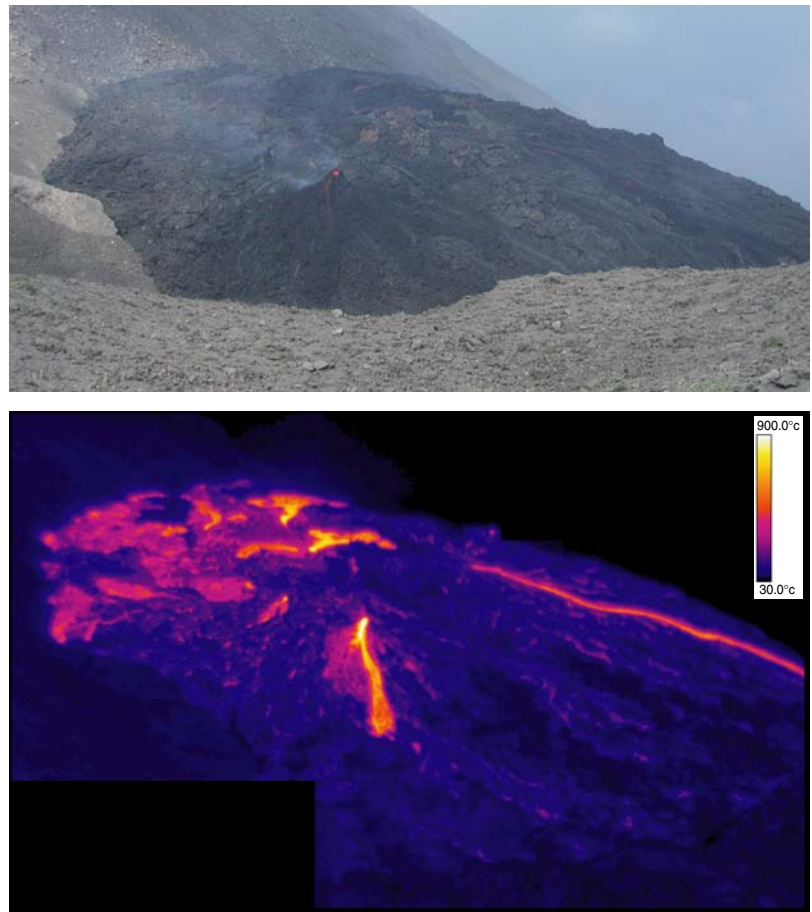
effusion rate of  $\sim 0.4 \text{ m}^3 \text{ s}^{-1}$ . During May 31–June 1, a major flow was active on the NE edge of the flow field (Unit D). A second zone of shorter, bifurcated flows was also active in the central zone of the flow field (Unit A). By June 1 a second zone of bifurcated flows had developed on the SW edge of the flow field (Unit B). It is possible that the subsequent robbing of supply from the D unit caused this flow to die out by June 2. An effusion rate surge on June 3 resulted in a complex braided flow field with at least 11 active units active across the central and SW sectors of the flow field (Units A and B). This may have marked a reorganization in the flow field, because thereafter activity became localized to the central sector (SW edge, Unit A) with only minor activity elsewhere (Table 2).

#### Flow dimensions and rheology

Flow dimensions on June 1 were typical of all those encountered during our study period. On this day units D, A and B were all active (Table 2).

Unit D extended 423 m and was fed by a single master channel 6.5 m wide. In the distal section the flow broadened to 19–29 m across, and had a 7.8 m wide central plug bounded by marginal shear zones. The previous morning (May 31) this flow had been just 266 m long. Thus the flow front had extended 160 m over a 24 h period, giving a time averaged flow front advance rate of  $0.002 \text{ m s}^{-1}$ . Unit A was fed by a tube that bifurcated at the head of the Sciara to feed two 'a'a flows. The longer of the two extended 499 m from the vent, and was fed by 5–7 m wide channel

**Fig. 3** Co-located digital photograph and FLIR image of the shield (June 1, 2003). View is looking SW towards the crater trench and shows (1) prominent hornito with summit vent feeding flank flow, (2) Active and cooling pahoehoe pads in the SW sector, and (3) active channels extending NE to feed the active flow field



that fed a distal ‘a’ lobe 22 m wide. This unit had been just 145 m long on the previous day. Thus the flow front advance of 354 m gives a time averaged flow front advance of  $0.004 \text{ m s}^{-1}$ . The shorter flow was 304 m long, was fed by a 1–4 m wide channel and comprised a 13 m wide distal lobe. Unit B also comprised two lobes extending 328 and 250 m from the vent. The shorter lobe was 13 m wide in the distal section, whereas the longer lobe was 22 m wide and displayed a 4 m wide central plug.

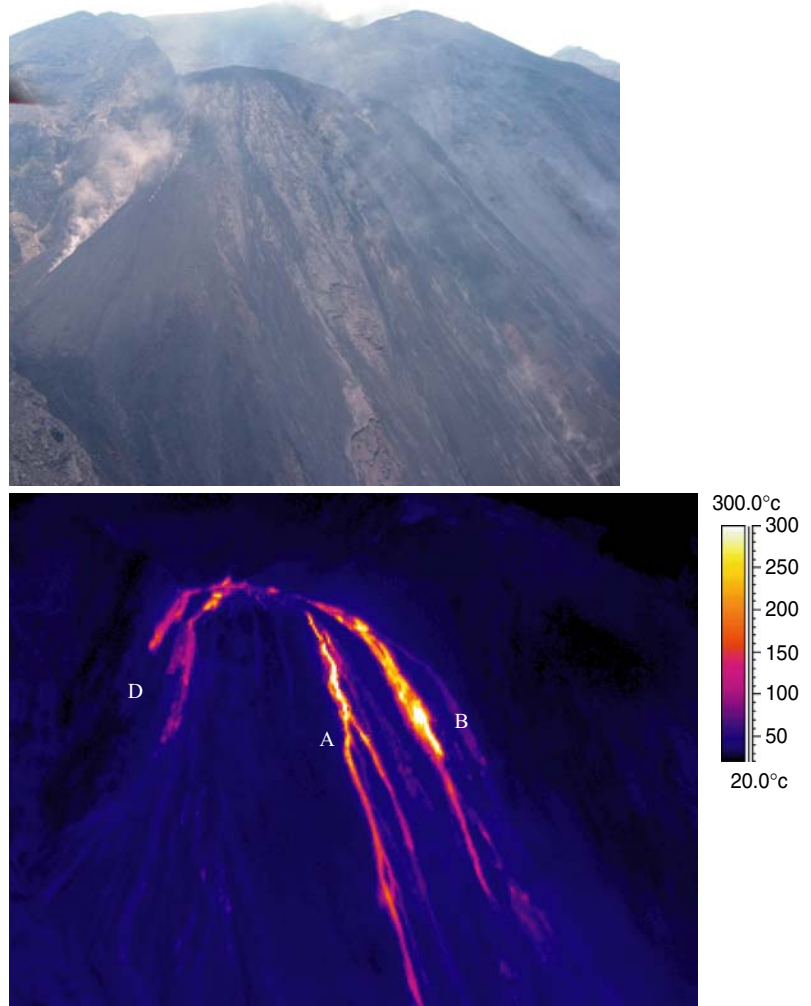
Flow velocities in the channels were of the order of a few centimeters per second ( $0.1\text{--}0.01 \text{ m s}^{-1}$ ), in spite of the extreme slope on which the flows were emplaced. Following Eq. (11), such low velocities are consistent with viscosities in the range  $10^5\text{--}10^6 \text{ Pa s}$ . These viscosities are also consistent with measured lava temperatures, where maximum surface temperatures of  $800\text{--}900^\circ\text{C}$  were obtained. The core temperature is easily  $100^\circ\text{C}$  higher, but even temperatures of  $1000^\circ\text{C}$  are consistent with viscosities of  $10^6 \text{ Pa s}$  (Shaw 1969).

#### Effusion rates

The effusion rate calculated by FLIR imagery gave an average over the 17 day study period of  $0.38\pm 0.25 \text{ m}^3 \text{ s}^{-1}$ . Anomalously high effusion rates occurred on June 1 and 3,

associated with two short lived ( $<24 \text{ h}$  long) pulses in the effusion rate (Fig. 5). During these surges, effusion rates peaked at  $0.8\pm 0.4$  and  $\sim 1.2\pm 0.6 \text{ m}^3 \text{ s}^{-1}$  on the two dates respectively. As described above, the first of these two surges was associated with a marked increase in the length of units A and D (Fig. 5). Although the second surge did not force such an obvious increase in flow length, it did result in a reorganization of the flow field. Following this reorganization, the effusion rates followed a trend of decline from a level around  $0.4 \text{ m}^3 \text{ s}^{-1}$  during June 4–8 to  $\sim 0.3 \text{ m}^3 \text{ s}^{-1}$  during June 9–16. Flow lengths at Unit A did not mimic this decline and instead remained fairly stable at  $\sim 450 \text{ m}$  during June 4–16 (Fig. 5). However, the reduction in supply may explain a reduction in activity, where activity at Units B and D declined significantly after June 4, with lava flow activity becoming focused at Unit A only (Table 2 and Fig. 5). In this case, the reduction in flow length at Unit B may have resulted from a gradual reduction in supply to this unit, while supply to Unit A was maintained at a similar level. In such a complex flow field, simple relationships between effusion rate and flow length may therefore be complicated. We note also that on such a steep slope a relationship between effusion rate and flow length may be further complicated by flow front collapse.

**Fig. 4** Co-located digital photograph and FLIR image of the shield (June 2, 2003). View is looking SE from an altitude of  $\sim 750$  m towards the shield and crater trench and shows (1) channel fed ‘a’ flow at Units A and B (to feed hot grain flow from the crumbling flow fronts), and (2) cooling flows at Unit D



## Discussion

The error in our effusion rate estimates is quite large, being nearly the scale of the measurement itself, but is comparable to error in field-based effusion rate measurements (Calvari et al. 2002; Harris and Neri 2002; Sutton et al. 2003). The reason for this lies in our lack of constraint on the input parameters of the model, where there are large uncertainties in input factors such as the convective heat transfer coefficient and the role of basal conduction (Table 1). Hence we prefer to give effusion rates over a broad range that takes into account these uncertainties (e.g. Fig. 5). Improved constraint of these input parameters is necessary if we are to reduce this range. However, comparing the effusion rate estimate of  $0.56 \text{ m}^3 \text{ s}^{-1}$  obtained on May 31 using channel dimensions with the thermally-derived range of  $0.23\text{--}0.87 \text{ m}^3 \text{ s}^{-1}$  indicates that the thermally-derived range is centered on the independent measure. Regardless of the range in our error, relative change in the effusion rates correlates with observed changes in flow length, area and activity; thus trends in the thermally-derived time series appear valid.

The mean effusion rates obtained here ( $0.38 \pm 0.25 \text{ m}^3 \text{ s}^{-1}$ ) are extremely similar to the eruption rate during the major last effusive eruption of Stromboli during 1985–86. For the 1985–86 eruption we obtain a time averaged eruption rate of  $0.34 \pm 0.05 \text{ m}^3 \text{ s}^{-1}$  from volume data given in Rossi and Sbrana (1988) and Nappi and Renzulli (1989). In addition, Harris et al. (2000) obtained  $0.31 \pm 0.2 \text{ m}^3 \text{ s}^{-1}$  from satellite thermal data during the 1985–86 eruption. These values, in turn, are comparable to the time-averaged supply to the shallow system of  $0.1\text{--}0.6 \text{ m}^3 \text{ s}^{-1}$  calculated from thermal and gas flux data by Allard et al. (1994) and Harris and Stevenson (1997). The similarity between the erupted fluxes during these effusive phases and the time-averaged supply during normal, persistent (non-effusive, Strombolian) activity, leads us to suggest that, during the study period, the eruption comprises bleeding of the conduit at a flux typical for Stromboli. The difference between the non-effusive and effusive phases is that the ascending (supplied) volume is not erupted in the former case, but instead degasses and descends in the convecting conduit (Allard et al. 1994; Harris and Stevenson 1997; Francalanci et al.

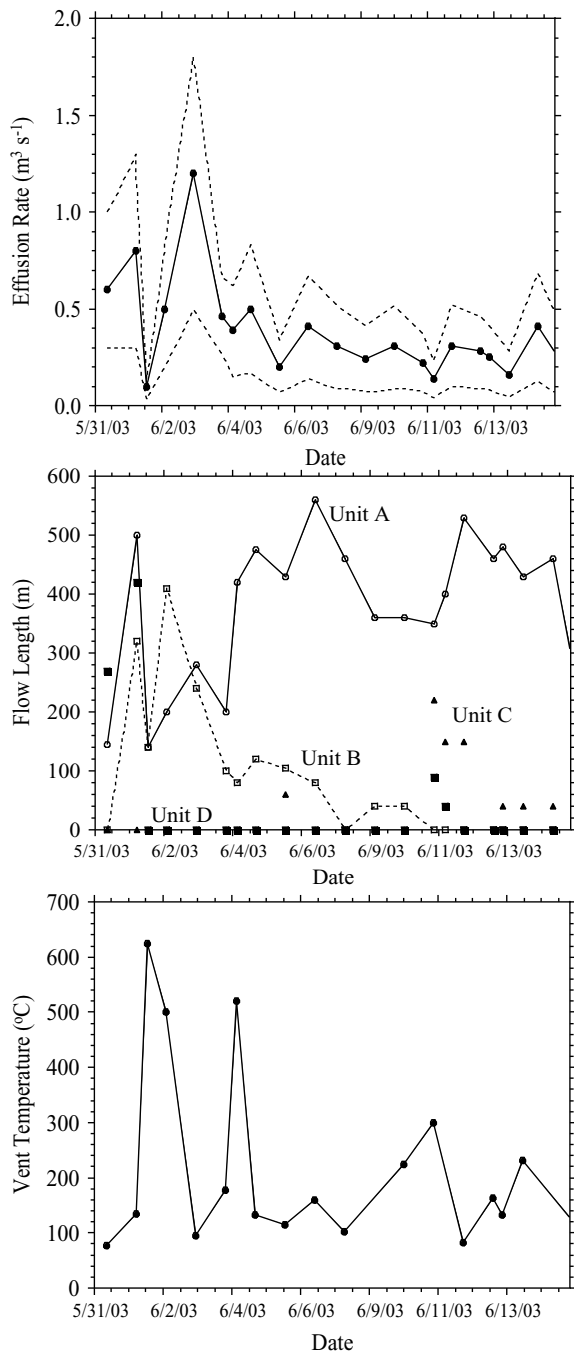


**Fig. 5** Time series of FLIR-derived (a) effusion rates, (b) flow lengths, and (c) NE crater vent temperatures

1999), whereas the ascending flux is erupted in the latter case.

In addition, the effusion rate pulses can be explained within the geometry of the shallow system. If, for example, we take a peak effusion rate on June 3 of  $\sim 1.2 \text{ m}^3 \text{ s}^{-1}$  the driving pressure ( $\delta p/\delta x$ ,  $p$  = pressure,  $x$  = along-dyke distance) to give this peak effusion rate can be calculated from (Kauahikaua et al. 1996):

$$E_r = (-\pi r^4/8\eta)(\delta p/\delta x) \quad (12)$$

in which  $r$  is the conduit radius. Using a plausible value of 2 m for the radius of the dyke extending from the central column below the crater terrace to the satellitic shield with  $10^3$ – $10^4 \text{ Pa s}$  for the viscosity of the magma in the shallow system (Ripepe and Gordeev 1999), we obtain  $\delta p/\delta x \sim 2 \times 10^4 \text{ Pa m}^{-1}$ . Thus, for a 250 m long dyke (the distance between the center of the NE crater and the center of the shield) we estimate a total overpressure ( $P$ ) of  $\sim 5 \text{ MPa}$ . This gives a column height ( $h$ ) of  $\sim 200 \text{ m}$  (from  $P = h \rho g$ , assuming  $\rho$  to be constant at  $\sim 2600 \text{ kg m}^{-3}$ ), which is approximately equal to the elevation difference between the satellitic shield and the floor of the NE crater. Interestingly, the temperature of vents in the NE crater was observed to rise prior to this effusion rate peak (Fig. 5), consistent with such an increase in the column height necessary to obtain the required driving pressure.

The 2–3 orders of magnitude difference in viscosity between the lava from the external system (lava flows at  $10^5$ – $10^6 \text{ Pa s}$ ) and the values needed and reported to effectively model the magma in the conduit ( $10^3$ – $10^4 \text{ Pa s}$ ) is not surprising. Lava is thixotropic, and at low stresses and strain rates, its viscosity will be high. Indeed, the effusion rates measured here were low and, in spite of the steep slope, the lava resisted flow, often collapsing at the flow front. However in the conduit, under pressure with a higher strain rate, it is reasonable to expect magma viscosities to be lower by 2 or more orders of magnitude due to higher volatile content, higher temperature and lower crystallinity.

## Conclusions

An effective method to calculate lava effusion rates was developed during June 2003 at Stromboli to aid in the monitoring effort at this volcano. In this test case, a fortuitous sampling geometry allowed us to acquire thermal imagery from effectively a near-vertical orientation from a low altitude and using a single image. However, our approach illustrates the utility and considerations required when using hand held thermal imagers to measure and monitor active lava flow fields. This technology has the potential to provide a high temporal resolution method to quickly, easily and safely measure lava effusion rates. Such data may then be linked to other data sets, such as gas flux, infrasound, and seismic data, to contribute to improved understanding of the dynamics of an effusive volcanic system.

**Acknowledgements** This work was supported by NSF grant EAR-0207734 and a grant from the United States Geological Survey. We are extremely grateful to the Italian Civil Protection and the pilots of Air Walser for facilitating and supporting our work on Stromboli, and to Lionel Wilson and an anonymous reviewer for providing two thorough reviews.

**Table A1** Parameters output by MATLAB software

Parameter	Units	Definition and Derivation
Area	m <sup>2</sup>	Lava area from sum of all lava pixel areas
$Q_{\text{rad}}$	W	$Q_{\text{rad}}$ for total lava area from sum of $Q_{\text{rad}}$ for each lava pixel
$Q_{\text{conv1}}$	W	$Q_{\text{conv}}$ for total lava area using $h_c=10 \text{ W m}^{-2} \text{ K}^{-1}$
$Q_{\text{conv2}}$	W	$Q_{\text{conv}}$ for total lava area using $h_c=100 \text{ W m}^{-2} \text{ K}^{-1}$
$Q_{\text{cond}}$	W	$Q_{\text{cond}}$ calculated using lava area and Table 1 values
$E_r1$	m <sup>3</sup> s <sup>-1</sup>	$E_r$ using $Q_{\text{rad}}+Q_{\text{conv1}}$ , $\Delta T=150$ ( <b>minimum end member</b> )
$E_r2$	m <sup>3</sup> s <sup>-1</sup>	$E_r$ using $Q_{\text{rad}}+Q_{\text{conv1}}$ , $\Delta T=250$ ( <b>intermediate end member</b> )
$E_r3$	m <sup>3</sup> s <sup>-1</sup>	$E_r$ using $Q_{\text{rad}}+Q_{\text{conv2}}$ , $\Delta T=150$ ( <b>intermediate end member</b> )
$E_r4$	m <sup>3</sup> s <sup>-1</sup>	$E_r$ using $Q_{\text{rad}}+Q_{\text{conv2}}$ , $\Delta T=250$ ( <b>intermediate end member</b> )
$E_r5$	m <sup>3</sup> s <sup>-1</sup>	$E_r$ using $Q_{\text{rad}}+Q_{\text{conv2}}+Q_{\text{cond}}$ , $\Delta T=150$ ( <b>intermediate end member</b> )
$E_r6$	m <sup>3</sup> s <sup>-1</sup>	$E_r$ using $Q_{\text{rad}}+Q_{\text{conv2}}+Q_{\text{cond}}$ , $\Delta T=250$ ( <b>maximum end member</b> )

**Table A2** Parameters output by Thermacam Researcher software

Parameter	Units	Definition and derivation
Area	%	Area greater than threshold expressed as a percent of the entire image
IFOV	m	Pixel width
Area	m <sup>2</sup>	Lava area
Tav	°C	Average temperature from all lava pixels [= $(T_{\text{min}}+T_{\text{max}})/2$ ]
$Q_{\text{rad}}$	W	$Q_{\text{rad}}$ for total lava area
$Q_{\text{conv}}$ (min)	W	$Q_{\text{conv}}$ for total lava area using $h_c=10 \text{ W m}^{-2} \text{ K}^{-1}$
$Q_{\text{conv}}$ (max)	W	$Q_{\text{conv}}$ for total lava area using $h_c=100 \text{ W m}^{-2} \text{ K}^{-1}$
$Q_{\text{cond}}$	W	$Q_{\text{cond}}$ calculated using lava area and Table 1 values
$E_r$ (min)	m <sup>3</sup> s <sup>-1</sup>	$E_r$ using $Q_{\text{rad}}+Q_{\text{conv}(\text{min})}$ $DT=150$ ( <b>minimum end member</b> )
$E_r$ (max)	m <sup>3</sup> s <sup>-1</sup>	$E_r$ using $Q_{\text{rad}}+Q_{\text{conv}(\text{max})}+Q_{\text{cond}}$ $DT=250$ ( <b>maximum end member</b> )

## Appendix A

### MATLAB software

The MATLAB software (written by MP) ingests a FLIR image or image mosaic and then, using the lava temperature threshold, identifies all lava pixels. Next, on a pixel-by-pixel basis, the software calculates the radiative and convective heat losses for each pixel using the pixel temperature and area. Total heat loss for the whole lava flow is then obtained by summing all of the individual pixel heat losses. The software finally outputs the parameters given in Table A1.

### Thermacam Researcher software

Given the limits of the Thermacam Researcher software, our software (written by JD) approach has to be slightly less sophisticated. Mainly, we are unable to make a pixel-by-pixel analysis. Thus our approach is modified as follows. Firstly, we identify lava area greater than the defined temperature threshold. Secondly, we obtain a median temperature using all lava pixels. Thirdly, we calculate the heat losses using the median temperature and lava area. Finally, we use the heat loss range to output an effusion rate range. The software thus outputs the parameters given in Table A2.

When compared using the same image, the two sets of software give comparable results, with the Thermacam software giving a narrower range of effusion rates that fall within the MATLAB-derived range.

## References

Allard P, Carbonnelle J, Metrich N, Loyer H, Zettwoog P (1994) Sulphur output and magma degassing budget of Stromboli volcano. *Nature* 368:326–330

- Calvari S, Neri M, Pinkerton H (2002) Effusion rate estimations during the 1999 summit eruption on Mount Etna, and growth of two distinct lava flow fields. *J Volcanol Geotherm Res* 119:107–123
- Calvari S, Andronico D, Burton MR, Dehn J, Garfi G, Harris A, Lodato L, Patrick M, Spampinato L (2005) Volcanic processes during the 2002–2003 flank eruption at Stromboli volcano detected through monitoring with a handheld thermal camera. *J Geophys Res*
- Crisp J, Baloga S (1990) A method for estimating eruption rates of planetary lava flows. *Icarus* 85:512–515
- Dehn J, Patrick MR, Harris AJL, Ripepe M, Calvari S (2004) Handheld infrared imaging of strombolian eruptions. *Bull Volcanol: in review*
- Francalanci L, Tommasini S, Conticelli S, Davies GR (1999) Sr isotope evidence for short magma residence time for the 20th century activity at Stromboli volcano, Italy. *Earth Plan Sci Lett* 167:1–69
- Harris AJL, Neri M (2002) Volumetric observations during paroxysmal eruptions at Mount Etna: pressurized drainage of a shallow chamber or pulsed supply? *J Volcanol Geotherm Res* 116:79–95
- Harris AJL, Stevenson DS (1997) Magma budgets and steady-state activity of Vulcano and Stromboli volcanoes. *Geophys Res Lett* 24:1043–1046
- Harris AJL, Butterworth AL, Carlton RW, Downey I, Miller P, Navarro P, Rothery DA (1997) Low cost volcano surveillance from space: case studies from Etna, Krafla, Cerro Negro, Fogo, Lascar and Erebus. *Bull Volcanol* 59:49–64
- Harris AJL, Flynn LP, Keszthelyi L, Mougins-Mark PJ, Rowland SK, Resing JA (1998) Calculation of Lava Effusion Rates from Landsat TM Data. *Bull Volcanol* 60:52–71
- Harris AJL, Murray JB, Aries SE, Davies MA, Flynn LP, Wooster MJ, Wright R, Rothery DA (2000) Effusion rate trends at Etna and Krafla and their implications for eruptive mechanisms. *J Volcanol Geotherm Res* 102:237–269
- Jeffreys H (1925) The flow of water in an inclined channel of rectangular section. *Phil Mag* 49:793–807

- Kauahikaua J, Mangan M, Heliker C, Mattox T (1996) A quantitative look at the demise of a basaltic vent: the death of Kupianaha, Kilauea Volcano, Hawai'i. *Bull Volcanol* 57:641–648
- Kneizys FX, Shettle EP, Gallery WO, Chetwynd JH, Abreu LW, Selby JEA, Clough SA, Fenn RW (1983) Atmospheric transmittance/radiance: computer code LOWTRAN 6. Air Force Geophysics Laboratory, Environmental Research Paper 846, Hanscom AFB, MA
- Keszthelyi L, Denlinger R (1996) The initial cooling of pahoehoe flow lobes. *Bull Volcanol* 58:5–28
- Keszthelyi L, Harris AJL, Dehn J (2003) Observations of the effect of wind on the cooling of active lava flows. *J Geophys Res* 30:SDE 4-1–SDE 4-4
- Marchetti E, Ichahara M, Ripepe M (2004) Propagation of acoustic waves in a viscoelastic two-phase system: influence of gas bubble concentration. *J Volcanol Geotherm Res*: in press
- Nappi G, Renzulli A (1989) Stromboli. *Bull Volcanic Eruptions* 26:1–3
- Ripepe M, Gordeev E (1999) Gas bubble dynamics model for shallow volcanic tremor at Stromboli. *J Geophys Res* 104:10639–10654
- Patrick M (2002) Numerical modeling of lava flow cooling applied to the 1997 Okmok eruption: comparison with AVHRR thermal imagery. MSc thesis University of Alaska Fairbanks: 141 p
- Pieri DC, Baloga SM (1986) Eruption rate, area, and length relationships for some Hawaiian lava flows. *J Volcanol Geotherm Res* 30:29–45
- Rossi M, Sbrana A (1988) Stromboli. *Bull Volcanic Eruptions* 25:7–8
- Shaw HR (1969) Rheology of basalt in the melting range. *J Petrol* 10:510–35
- Sutton AJ, Elias T, Kauahikaua J (2003) Lava-effusion rates for the Pu'u 'Ö'ö-Kūpaianaha eruption derived from SO<sub>2</sub> emissions and very low frequency (VLF) measurements. USGS Prof paper 1676:137–148
- Wright R, Blake S, Harris A, Rothery D (2001) A simple explanation for the space-based calculation of lava eruptions rates. *Earth Planetary Sci Lett* 192:223–233
- Wooster MJ, Wright R, Blake S, Rothery DA (1997) Cooling mechanisms and an approximate thermal budget for the 1991–1993 Mount Etna lava flow. *Geophys Res Lett* 24(24):3277–3280